SMC-TR-95-44

AEROSPACE REPORT NO.
TR-95(5231)-8

Characteristics of Alumina Particles From Solid Rocket Motor Exhaust in the Stratosphere

15 September 1995

Prepared by

E. J. BEITING
Mechanics and Materials Technology Center
Technology Operations

Prepared for

SPACE AND MISSILE SYSTEMS CENTER
AIR FORCE MATERIEL COMMAND
2430 E. El Segundo Boulevard
Los Angeles Air Force Base, CA 90245

Space Technology Applications

THE AEROSPACE CORPORATION
El Segundo, California

This report was submitted by The Aerospace Corporation, El Segundo, CA 90245-4691, under Contract No. F04701-93-C-0094 with the Space and Missile Systems Center, 2430 E. El Segundo Blvd., Los Angeles Air Force Base, CA 90245. It was reviewed and approved for The Aerospace Corporation by S. Feuerstein, Principal Director, Mechanics and Materials Technology Center. John R. Edwards was the project officer for the program.

This report has been reviewed by the Public Affairs Office (PAS) and is releasable to the National Technical Information Service (NTIS). At NTIS, it will be available to the general public, including foreign nationals.

This technical report has been reviewed and is approved for publication. Publication of this report does not constitute Air Force approval of the report's findings or conclusions. It is published only for the exchange and stimulation of ideas.

John R. Edwards

John R. Edwards
SMC/CEV

REPORT DOCUMENTATION PAGE

Form Approved
OMB No. 0704-0188

Public reporting burden for this collection of information is estimated to average 1 hour per response, including the time for reviewing instructions, searching existing data sources, gathering and maintaining the data needed, and completing and reviewing the collection of information. Send comments regarding this burden estimate or any other aspect of this collection of information, including suggestions for reducing this burden to Washington Headquarters Services, Directorate for Information Operations and Reports, 1215 Jefferson Davis Highway, Suite 1204, Arlington, VA 22202-4302, and to the Office of Management and Budget, Paperwork Reduction Project (0704-0188), Washington, DC 20503.

1. AGENCY USE ONLY (*Leave blank*)

2. REPORT DATE
15 September 1995

3. REPORT TYPE AND DATES COVERED

4. TITLE AND SUBTITLE
Characteristics of Alumina Particles From Solid Rocket Motor Exhaust in the Stratosphere

5. FUNDING NUMBERS
F04701-93-C-0094

6. AUTHOR(S)
E. J. Beiting

7. PERFORMING ORGANIZATION NAME(S) AND ADDRESS(ES)
The Aerospace Corporation
Technology Operations
El Segundo, CA 90245-4691

8. PERFORMING ORGANIZATION REPORT NUMBER
TR-95(5231)-8

9. SPONSORING/MONITORING AGENCY NAME(S) AND ADDRESS(ES)
Space and Missile Systems Center
Air Force Materiel Command
2430 E. El Segundo Boulevard
Los Angeles Air Force Base, CA 90245

10. SPONSORING/MONITORING AGENCY REPORT NUMBER
SMC-TR-95-44

11. SUPPLEMENTARY NOTES

12a. DISTRIBUTION/AVAILABILITY STATEMENT
Approved for public release; distribution unlimited

12b. DISTRIBUTION CODE

13. ABSTRACT (*Maximum 200 words*)

Based on currently available data, a unified model for the particle size distribution, particle density, and geometrical dispersion for the alumina particles in the exhaust of a Titan SRM plume in the stratosphere is presented. The particle size distribution is found to be trimodal with Sauter mean diameters of 0.056, 1.0, and 3.6 μm for the small, medium, and large size modes, respectively. Nearly all the particles lie within the small size mode, but nearly all the mass lies in the large size mode. About two-thirds of the particle surface area available for heterogeneous chemical reactions is due to the large particle mode while most of the remaining surface area is due to the small particle mode. The light scattering characteristics of the plume were also explored. Mie scattering calculations were used to predict the local attenuation of the plume as a function of wavelength and the total attenuation of a beam of radiation through the plume making an arbitrary angle with respect to the axis of the plume and as a function of time after SRM passage for several wavelengths in ultraviolet, visible, and infrared spectral regions. These studies show that most of the attenuation is due to the large-size mode. An expression for the volume density of total area of the particles is derived in terms of known parameters and the Sauter mean diameter. Mie theory is then used to show that this Sauter mean diameter can be measured using a two-color transmissometer.

14. SUBJECT TERMS
Rocket plumes, Ozone depletion, Stratospheric particles, Optical particle detection

15. NUMBER OF PAGES
40

16. PRICE CODE

17. SECURITY CLASSIFICATION OF REPORT
UNCLASSIFIED

18. SECURITY CLASSIFICATION OF THIS PAGE
UNCLASSIFIED

19. SECURITY CLASSIFICATION OF ABSTRACT
UNCLASSIFIED

20. LIMITATION OF ABSTRACT

NSN 7540-01-280-5500

Standard Form 298 (Rev. 2-89)
Prescribed by ANSI Std. Z39-18
298-102

Preface

The author thanks J. A. Syage for useful discussions on LIDAR and TOMS measurements, B. B. Brady and L. R. Martin for information and discussions on their plume model, J. T. Knudtson for making the video tape of the K-10 available and (with D. R. Schulthess) providing information on the K-10 launch, and M. R. Denison for information on the altitude scaling of the small-scale eddy diffusion coefficient.

Contents

Figures

Tables

1.0 Introduction

Interest in the environmental effects of solid rocket motor (SRM) exhaust on the atmosphere has led to a number of recent studies. Models were developed that predicted perturbed chemistry in the upper atmosphere and, in particular, a transient ozone hole in the stratosphere.[1-8] Other than a brief mention of depressed ozone levels of a plume fly-through [9], no observational evidence exists of this effect. The ability to verify experimentally the predictions of these models has become a topic of considerable interest.[10-19] Most of the techniques proposed for these measurements are optical, therefore the ability to interpret the data collected by these instruments and even the feasibility of the techniques themselves depend on an *a priori* knowledge of the characteristics of the alumina (Al_2O_3) particles in the plume. For example, Mie scattering by the particles can affect the ability to recover *in-situ* ultraviolet absorption spectra [12], alter the interpretation of ground-based absorption data using a solar or stellar source [17], change the interpretation of TOMS [16] and HIROIG [18] data, and affect the feasibility of making LIDAR measurements. [11,14]

The particles also may play a role in the chemical interaction of the plume with the stratosphere through heterogeneous reactions.[2,7] For this reason, it is desirable to measure the total particle area available as a reaction surface. This measurement is required in addition to gas-particle adsorption/desorption kinetics and the number density of the gaseous chemical constituents of the plume to gain a true understanding of the stratospheric plume chemistry. The design of instruments to measure remotely (or in some cases by *in situ* techniques) the reaction surface area, not surprisingly, also requires foreknowledge of the particle sizes and density.

This report attempts to address these needs by gathering the best available data on SRM exhaust particles and plume dispersion in the stratosphere. This information is used to develop a model of specific particle density; that is, the particle number density as a function of particle size, altitude, position in the plume, and time after vehicle passage. Estimates of the reaction surface area and optical characteristics of the plume then are predicted based on this model. In addition, a straightforward optical technique to measure the total surface area per air volume is described. Much of the analysis presented here was taken from unpublished studies by the author addressing the problem of plume measurements. [12,13,19] This report extensively updates, augments, and presents the information in a more accessible form. Many of the calculations presented in these previous reports have been redone based on the most recent form of the particle model presented here. Some information on the plume dispersion measurements and feasibility of a flight transmissometer have not been included in this report.

2.0 Particle Composition and Morphology of the Plume

2.1 Measured Large-Particle Ambient Composition of the Stratosphere

The large-particle (> 1μm) composition of the stratosphere is briefly reviewed because it is the background against which particle measurements must be made and because it is a source of information for the large-particle distribution of SRM exhausts, which is missing from the SRM exhaust stratospheric database. As shown below, the particles that contribute most of the surface area available for chemical reaction are those with diameters greater than 1 μm.

Table I
Number Densities of Ambient Stratospheric Particles (m^{-3})
(from ref. 20)

Year	*Chondritic*	*Silicate*	*Al*	*Al'*	*Fe-S*	*Fe+S*	*CAS*	*Low-Z*	*Other*	*Total*
1976	0.010	0.030	0.004	0.018	0.007	0.004	0.002	0.002	0.013	0.089
1981	0.018	0.037	0.037	0.013	0.013	0.005	0.002	0.018	0.021	0.16
1984	0.017	0.22	0.71	0.15	0.051	0.051	0.002	0.27	0.22	1.7

Notes: Chondritic = extraterrestrial origin; Al = Aluminum and alumina components only; Al' = Primarily aluminum with lesser amount of other elements; CAS = calcium aluminum silicates. Activity and ablation of spacecraft material produces particles in the classes of Al, Al', silicate, Fe-S, Fe+S, low-Z, and other. Densities are in units of m^{-3}

A comprehensive analysis of ambient stratospheric particle data taken during the period of 1976-1984 is available, and data presented here are drawn from that report. [20] All data were collected between an altitude of 17 and 19 km with NASA WB-57F and U2-C aircraft using retractable solid inertial impaction collectors. All samples were analyzed for morphology, size, and chemical composition. Table I and Figs. 1 and 2 show some relevant results. The number densities shown are minimum values since the collector plate efficiency is less than 100% due to (smaller) particles flowing around the plate.

From Fig. 2, it is clear that nearly all the ambient Al particles have diameters of less than 4 μm. Noting that the total particle density in the SRM plume about ten minutes after vehicle passage is approximately 10^{10} m^{-3} (see Section 2.3.1.2 below) and that the small particles have a density of 10^6 times greater than particles with diameters greater than 1 μm (see Fig. 3 below), we see that the early large particle density in the plume is ~ 10^4 m^{-3}, which is a factor of 10^4 - 10^5 greater than the ambient large-particle density. Thus, the ambient particle density will contribute negligibly to plume particle measurements and effects at early times. The time required for this early density to disperse to the ambient large-particle density is discussed in Section 2.3.

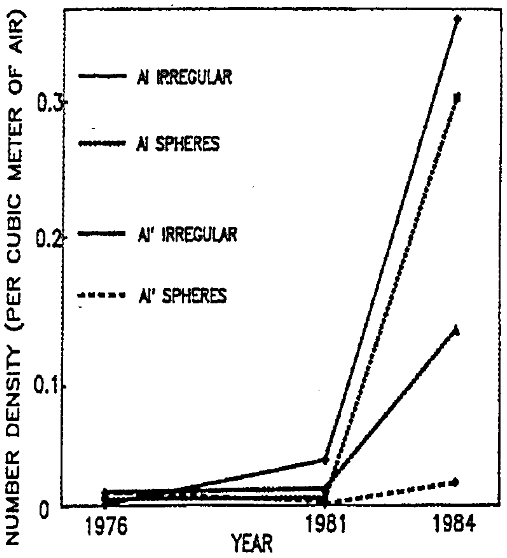

Figure 1. Partition of ambient large Al and Al' particles at 17-19 km altitude during the period 1976-1984 (from ref. 20).

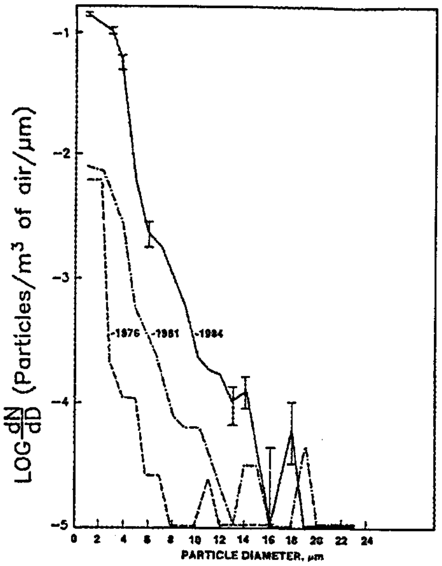

Figure 2. Total large Al ambient particle size distribution at 17-19 km altitude during the period 1976-1984 (from ref. 20).

Approximately an order of magnitude increase in total large solid particle number density and a factor 20 increase of Al and Al' particle number density of the stratosphere occurred during the study period. This increase is attributed to SRM exhaust and rocket and satellite debris. [20] The main source of the Al and Al' particles is rocket motor exhaust and ablating spacecraft. About half the 1984 Al particles are spherical (see Fig. 1), and these spherical particles are attributed solely to SRM exhaust. If we assume that the spherical particle size distribution of the Al particles is not grossly different from that of the nonspherical Al distribution, then the 1984 curve in Fig. 2 can be used to calculate estimated mean diameter of the large particles in the SRM plume. This is done in section 2.2.

2.2 Particle Characteristics in SRM Plumes

Particle size measurements have been made in the motors of subscale rockets [21-25], in the ground clouds of a Titan [26,27] and the STS [28], in the upper troposphere plume of the STS [28-31], in the stratospheric plume of a Titan [27], and in the plume of an Atlas [26]. Particle density measurements were made in the tropospheric plumes of the STS [29,31], and the ground cloud [26,27] and stratospheric plume [27] of a Titan. Particle morphology was studied in the ground clouds of a Titan [27] and the STS [28], in the stratospheric plumes of a Titan [27], and the tropospheric plumes of the STS [28,30-32]. Chemical composition was studied of the particles collected in stratospheric plumes of a Titan [27] and the tropospheric plumes of the STS [32] as well as from plumes of other small rockets (PAM D-II, IUS, Peacekeeper Stage II) [33]. Studies of the environmental effects of particles from STS plumes in the troposphere [34] and stratosphere [34,35] have also been made.

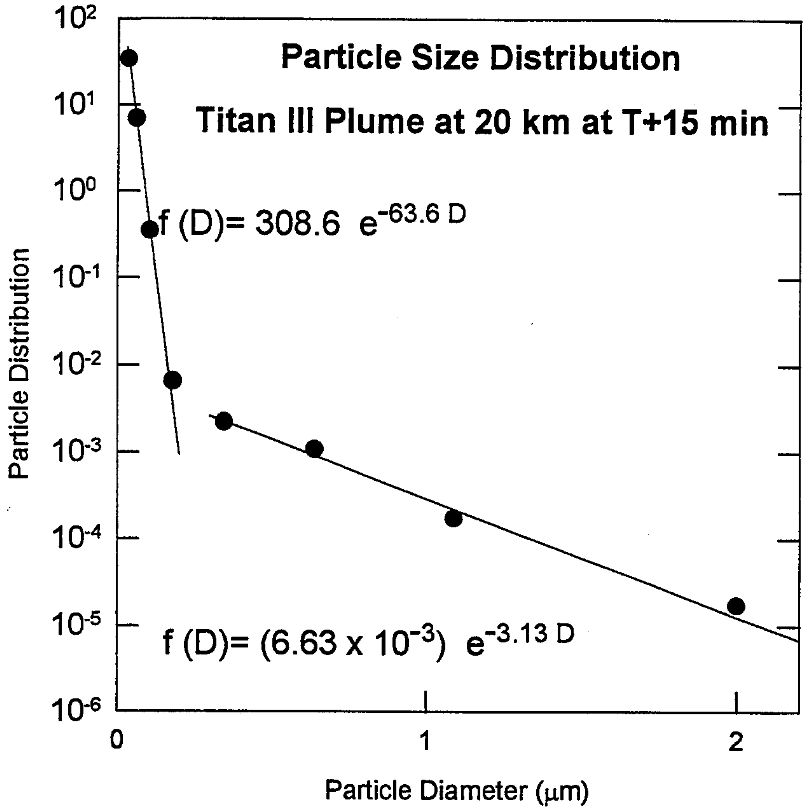

Figure 3. Fits to stratospheric Titan III plume data of Strand *et al.* [27].

The relevant results from these works are:

1) The particle size distribution extends from below 0.03 μm to approximately 10 μms and is probably trimodal in the stratosphere in this size range for large rockets. [27,31] At stratospheric altitudes, particle size increases with time (during the first few minutes after vehicle passage) for particles with diameters between 0.3 μm and 1.33 μm due to condensation of vapors or agglomeration. [27] Particle size decreases with increasing rocket motor size. [23]

2) The particles are spherical in shape and have a composition of Al_2O_3 with trace amounts of other elements (K, Na, Ti, Fe, Si) and small surface contamination of HCl. [27, 30-32,34] The density of the particles varied between 1.5 and 3.5 gm cm^{-3}, with larger particles tending to have lower densities (presumably because they are hollow or porous). [27,34]

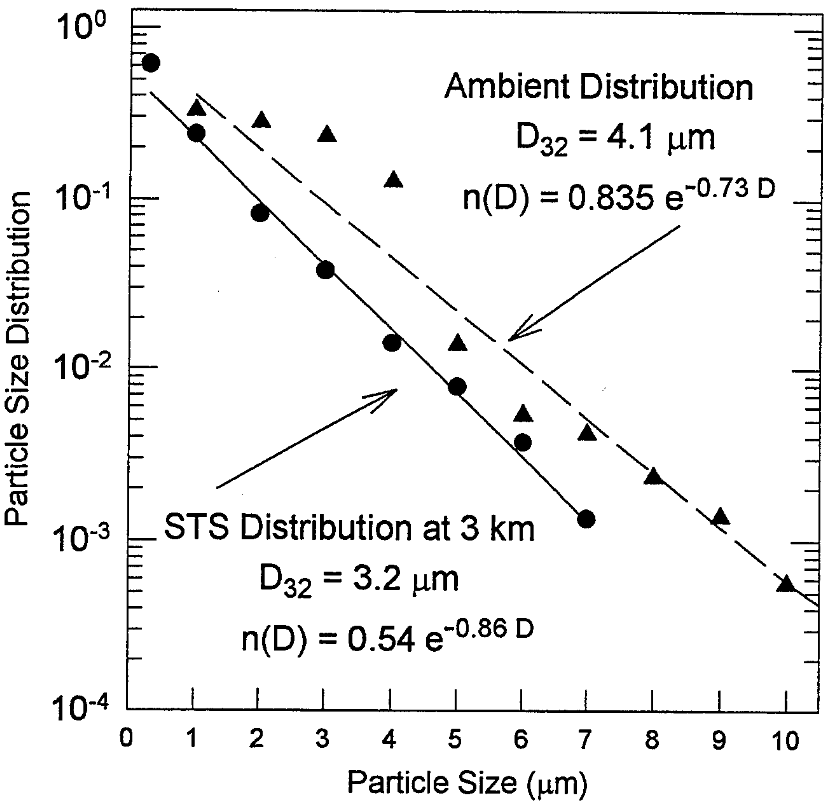

Figure 4. Fits to ambient stratospheric particle data of Zolensky *et al.* [20] and tropospheric STS plume particle data of Cofer et al. [31]. The Sauter mean diameter, D_{32}, is defined in Eq. 18 below.

3) Most of the Al_2O_3 is cubic gamma phase, and the ratio of gamma to hexagonal alpha phase is about four. [33] The small particles tend to be in the gamma phase. [36]

4) In the troposphere between 3 and 7 km, the particle size distribution is independent of altitude for particles with diameters greater than 1 μm. [31]

5) Particle size distribution is a function of radial position in the plume. The smallest particles are uniformly distributed, but the larger particles are confined to the plume center. [24] Nozzle/plume flow-field codes predict that particles larger than 1 μm are concentrated along the plume centerline, and particles as small as 1 μm cannot follow the flow along the diverging nozzle wall.[37,38]

There is only one report of *in-situ* observations of particle size distribution and density of large SRMs (Titan IIIs) in the stratosphere. [27] These measurements were restricted to particle diameters below 2 μm and were taken using two different types of instruments (oil wire impactor and sticky tape). Both instruments measured identical distributions. The sticky tape measurements are plotted in Fig. 3 where we fit them to exponential functions. The distribution is clearly bimodal with Sauter mean diameters of 0.056 μm and 1.0 μm and slopes of 63.6 and 3.13, respectively.

Since there are no measurements of the particle size distributions (> 2μm) from SRMs for large particles in the stratosphere, a distribution function for this mode is created from the ambient stratospheric Al particle measurements and the tropospheric STS plume particle measurements. The large particle size distribution of Space Shuttle plumes was taken in the troposphere. [31] The distribution measured at 3 km is plotted and fit to an exponential curve in Fig. 4. It is clearly monomodal and has a Sauter mean diameter of 3.2 μm and slope of 0.86. The distributions measured at higher altitudes (up to 7 km) were similar. The 1984 ambient stratospheric size distribution taken from Fig. 2 is also shown in Fig. 4 and displays a nearly identical distribution (D_{32} = 4.1 μm and slope 0.73) Here D_{32} is the volume-weighted-to-area-weighted (Sauter) mean diameter (see Eq. 18). Since the ambient distribution plotted in Fig. 4 is due primarily to large SRM exhaust, and the tropospheric plume measurements did not change with altitude up to 7 km, one could argue that the stratospheric large-particle distribution has a mean diameter and slope between those shown in Fig. 4. Therefore for modeling purposes, the large particle distribution will be taken to have a D_{32} of 3.6 μm and a slope of 0.8. Note that this slope is more than twice the slope of the intermediate distribution given in Fig. 3, indicating a trimodal particle distribution for large SRMs in the stratosphere.

2.3 Stratospheric Plume Diameters and Expansion Rate

A vital parameter required for the measurement of the properties of particle or chemical species in an SRM stratopheric plume is an estimate of the plume dispersion rate. A rapidly expanding plume will quickly lower the particle densities (and chemical concentrations), making real-time detection difficult. Little data are available on plume expansion in the statosphere. The data that are available show only early rates (0-600 s). These expansion rates are generally an order of magnitude higher than those generally attributable to large-scale eddie diffusion. In this section, we first review the available data, then we review plume dispersion models, and finally we compare the data to the models.

2.3.1 Observations

There is only one previous measurement of SRM plume expansion. In addition to this measurement, we infer plume size and expansion rate from the the U-2 flythrough data of Strand *et al*. Finally new observations of plume expansion are reported here.

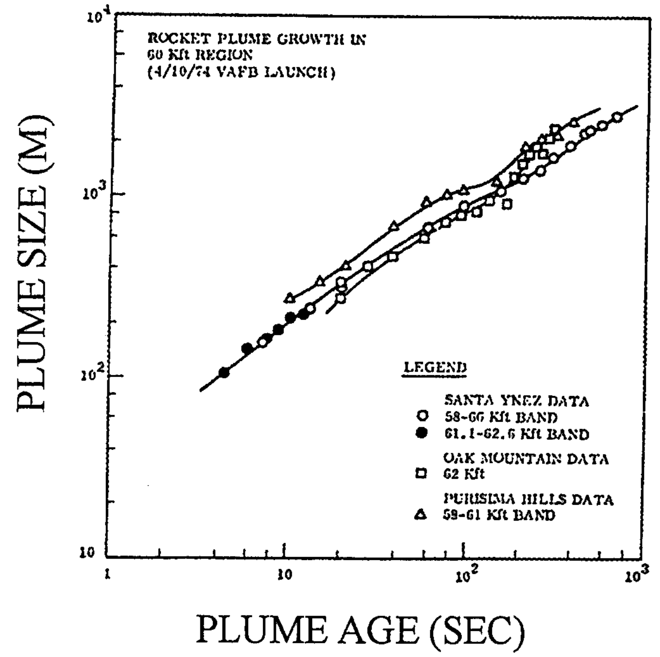

Figure 5. Plume data of Hoshizaki [39].

2.3.1.1 Plume Growth Data of Hoshizaki

A conscientious (but not exhaustive) search of the literature found only one observation of SRM plume expansion in the stratosphere. This measurement observed the first few minutes of plume growth. Hoshizaki [39] reported plume growth data of a 4 Oct 1974 launch from VAFB. These data are shown in Fig. 5. These measurements were taken from photographs of a "large solid rocket booster" (presumably a Titan III) by Lockheed, under contract to NASA/Ames, using cameras located at four ground sites surrounding the launch pad. The photographs were taken of the plume for approximately 10 minutes, and used to measure plume expansion between altitudes of 18 and 19 km. The data show a linear expansion rate of about 0.3 km/min during this time period.

2.3.1.2 U-2 Fly-through of Titan IIIc Plumes

In 1975, data on alumina particle density and size distribution were obtained from two Titan IIIc launches (May 20, 1975 and June 8, 1975). [27] On each of these launches, a U-2 aircraft made two traversals of the plume at times T+7 and T+13 min (May 20) and T+6.5 and T+13.5 min (June 5) at an altitude of 19 km. Measurements of total particle number densities at these times yielded values of 10^9 and 10^8 m^{-3} (May 20) and 10^{10} and 10^9 m^{-3} (June 6). The authors state that 10^{10} m^{-3} is the theoretically predicted value for the particle number density at early times. Thus they find that the particle density falls an order of magnitude for a plume expansion time of a factor of two. This rate of expansion is consistent with a plume expanding in three dimensions at a linear expansion rate or in two dimensions at an expansion rate of $t^{3/2}$. All data and most models show a linear expansion with time. All models assume two-dimensional expansion.

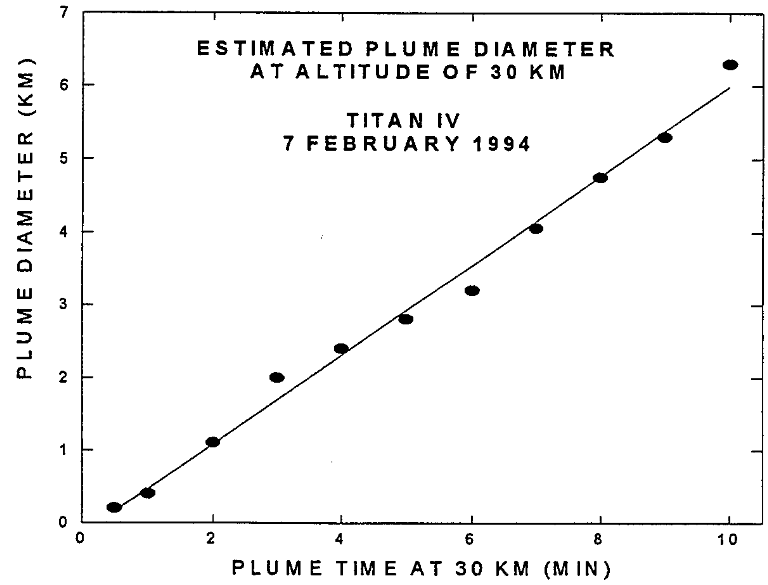

Figure 6. Estimated plume diameter at an altitude of 30 km from the K-10 launch of a Titan IV.

An estimate of the cross-sectional area of the plume (and hence the diameter) can be obtained by dividing the mass flow rate of the Titan IIIc vehicle (16 gm/cm of vehicle track at an altitude of 19 km) by the average mass density. The average mass density can be calculated based on the model presented in Section 2.4 below (see Table IV in Section 2.5). This model is normalized to the particle density measurements of the U-2 flythroughs. Averaging the mass over an area given by a radius defined by the distance required for the particle density to fall to e^{-2} of its peak value yields a diameter of 5 km. Using an averaging distance set by an e^{-1} density falloff yields a diameter closer to 4 km.

Additional information presented in Ref. [27] allows another estimate of the plume diameter to be made. The work notes that the time required to fly through the plume was between five and ten seconds. This corresponds to a distance of 1 - 2 km since the U-2 speed is 200 m/s. Interpretating these distances as the plume diameters is complicated by several factors: the horizontally flying aircraft traversing a nonvertical plume will measure a distance greater than the diameter; traversing a cord will measure a distance smaller than the diameter; and criterion for the detection of the edge of the plume is unidentified. Nevertheless, making this association yields an approximate plume diameter of 1.5 km at T+10 min at an altitude of 19 km.

2.3.1.3 Titan IV Videotape Observations

A recent video taken of a Titan IV launch (K-10, 7 Feb. 94) presents the possibility of estimating early plume diameters and expansion rates. [40] This flight was launched from Launch Complex 41 (LC-41) from KSC and was observed from universal camera site 2 (UCS2), a distance of 7.6 km from LC-41. An infrared and a visible camera tracked the flight to 30 km

Table II

Model Resultsof Watson *et al.* [41]

Time	Width (km)
0	0.024
1 hr	1.4
5.6 hr	14
1 day	96
10 days	1260
1 month	3700

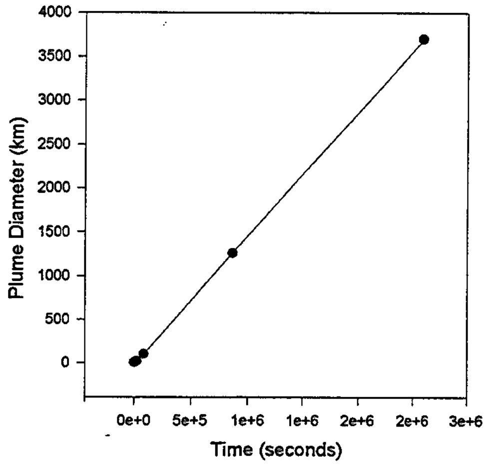

Figure 7. Temporal dependence of cloud diameter of a chemical release at an altitude of 40 km (data from ref. 41).

(T+96 s) and then held position to observe the plume. The known horizontal field-of-view (FOV) of the IR camera through the 3X telescope (0.1047 radian) permitted the calibration of the visible camera FOV (0.14 radian H; 0.11 radian V) using structures observed by both cameras before the launch. At T+96 s, the surface distance from UCS2 to the rocket was 33.8 km, resulting in a 45.2 km range for the 30 km altitude. Thus the FOV of the camera was 6.6 km H and 5.0 km V. The horizontal viewing angle was 11.6° off of alignment with the trajectory.

The diameter of the plume was estimated by marking the 30 km position on the screen and observing the expansion of the plume in a direction normal to the centerline of the plume. The plume was observed to expand symmetrically around its centerline. After four minutes, the lower edge of the plume expanded off the bottom of the screen, and diameters were subsequently measured from the center of the expansion to the upper edge of the plume and doubled to obtain the diameter. Even though the day was clear, the plume was sufficiently dispersed to make it difficult to discern its edge after about ten minutes. The estimated diameters are shown in Figure 6. The diameter of the plume increases linearly with time at rate of approximately 0.6 km/min. The nearest measurement of local wind conditions were at 6 AM local time, whereas the launch was in the late afternoon. At 6 AM the wind speed was 5.9 m/s from 182° at an altitude of 28 km. [19]

2.3.2 Models

Three models of plume dispersion are reviewed. The first by Watson *et al.* is believed to be accurate for times longer than a few hours after launch (> 1 day). The second is the model of Denison *et al.*, which is based on the data of Hoshizaki and is thus verified for short times (10 min.). The third model is by Ross [8] and is designed for times intermediate to these periods.

2.3.2.1 The Model of Watson *et al.*

Watson *et al.* [41] made a study of Space Shuttle plume dispersion characteristics of F_2 and N_2O_4 in the stratosphere and mesosphere. Above an altitude of 100 km, plume dispersal is dominated by molecular diffusion. Below this altitude, dispersion is produced by both small- and large-scale eddies that can be parameterized in terms of an overall eddy transport coefficient. Using a theoretical model (based on an admittedly limited data base) previously developed [42], Watson *et al.* obtained a time scaling of the horizontal diffusion coefficient K_{yy} based on the model results at 100 km. At times less than 10^5 s, they state that this model may underestimate the horizontal plume dispersal rate due to an incorrect time evolution of K_{yy}.

The vertical dispersal (the main emphasis of Ref [41]) is two to three orders of magnitude less than this horizontal dispersal rate so the expansion proceeds primarily in two dimensions. Watson *et al.* used this model to calculate the plume width and densities at an altitude of 40 km at times of 0 s, 1 h, 5.6 h, 1 day, 10 days, and 1 month (Ref [41], Table 4). Due to uncertainties of K_{yy}, they state that the calculations of plume volumes are only accurate to an order of magnitude. Their results are shown in Table II and Fig. 7. These values indicate an initial expansion rate (0 - 1h) of 1.4 km/h (0.023 km/min) and at longer times a nearly linear expansion rate of 5.2 km/h. Brady and Martin [7] used the values shown in Table II to scale temporal dependence of the chemical concentrations in the plume and found a time dependence of the concentration given by

$$n(t) = \frac{n_0}{1+\left[\left(2\times10^{-3}\right)t\right]^{2.6}} \qquad \text{(t in seconds).} \tag{1}$$

The initial value of n_0 was scaled with local atmospheric pressure.

2.3.2.2 The Model of Denison *et al.* [2]

In their chemical model calculating local ozone depletion by solid rocket plumes, Denison *et al.* modeled the diffusion of the plume by solving the conservation equation in cylindrical coordinates,

$$\frac{\partial n}{\partial t} = K_{yy}\,\nabla^2 n = \frac{1}{r}\frac{\partial}{\partial r} r K_{yy}\frac{\partial n}{\partial r}, \tag{2}$$

where n is the number density, r is the radial coordinate, t is time, and K_{yy} is the diffusion coefficient. Using the plume size measurements of Hoshizaki [39] taken at an altitude of 18 km, they found the diffusivity to be scale dependent, where

$$K_{yy} = br\,, \tag{3}$$

and b = 1.75 m s^{-1}. Under this assumption, the solution of Eq. 2 for a line source is

$$n(r,t) = At^{-2} \exp(-r / bt), \tag{4}$$

where A is a normalization constant. This solution can be written

$$n(r,t) = n_0 \left(\frac{t_0}{t} \right)^2 \exp\left[-\frac{1}{b} \left(\frac{r}{t} - \frac{r_0}{t_0} \right) \right], \tag{5}$$

where n_0 is the particle number density at r_0 and t_0. Using the relation

$$\frac{n(r,t)}{n(r = R_i, t)} = e^{-2} \tag{6}$$

to define a radius, we find the time dependence of the plume radius is

$$R(t) = R_i + 2bt, \tag{7}$$

where R_i is the initial radius. Assuming $R_i = 5$ m, the plume diameters at 1 and 10 min are 430 m and 4.2 km, respectively. This diffusion model was also employed by Kruger [4] and secondarily by Brady and Martin [7] to calculate the local stratospheric ozone depletion by a solid rocket in their chemical kinetics models.

Table III

Plume Diameters from Ross [8]

Alt (km)	T+1.25 hr	T+4.25 hr
20	2.8	12
30	2.4	10
40	4.0	--

2.3.2.3 The Model of Ross

More recently, Ross [8] completed a model of a Titan IV SRM plume in the atmosphere that included a limited chemical reaction set and fluid dynamic mixing in the stratosphere for up to 8 h after launch. The model assumes cylindrical symmetry in a series of 1-km-thick layers and builds a three-dimensional model by permitting the layers to move independently according to their altitude-dependent zonal (E-W) and meridional (N-S) wind speeds. This model also parameterizes the transport in terms of an eddy diffusion coefficient using a time-dependent value of K_{yy} (m^2s^{-1}) = $0.01t(s)^{1.3}$, a value assumed to be independent of altitude. This work presents Al_2O_3 number densities at T+1.25 h and T+4.25 h for altitudes of 20, 30, and 40 km. Defining a radius at the $1/e^2$ density, the diameters inferred from the density plots of this model are given in Table III. These values indicate an expansion rate of about 3 km/h.

2.3.3 Comparison and Discussion

It is useful to compare the data of the early plume expansion with the dispersion models being employed by the plume chemistry models. Since the data were taken at different altitudes, this comparison requires some understanding of the altitude scaling of the small-scale eddy diffusion coefficient. The large-scale atmospheric eddy diffusion coefficient has received considerably more study for global atmospheric modeling. The scaling of the large vertical eddy diffusion coefficient K_{zz} with altitude between 18 and 40 km varies from being constant to increases of a factor of 25 (varying approximately with inverse atmospheric pressure) depending on the model. [41,43,44] Plots of the variation of large-scale K_{yy} as a function of altitude and latitude are given in ref. [41], which were taken from Ref. [43]. At a latitude of 30°, there is little variation of this parameter in the 20-40 km altitude range. Based on the data presented by Hoshizaki, Denison *et al.* found that the small-scale values of K_{yy} at ten minutes are two to three orders of magnitude smaller than those of the large-scale values. If the early linear growth rate continues unabated, one to two days are required before the values of the small-scale diffusivity reach the large-scale values. Therefore the applicability of these large-scale altitude variations of K_{yy} and K_{zz} to the small scale values of K_{yy} is highly questionable and the small-scale altitude variation must be considered unknown at this time.

Tropospheric measurements of the small-scale K_{yy} values at altitudes between 2 and 4 km of a nuclear debris cloud give values similar to (a factor of two less than) the stratospheric values noted here. [45] Given the large differences between the troposphere and the stratosphere, this must be taken as evidence that the altitude variation of small-scale K_{yy} is not large. A conservative approach to altitude scaling is to consider the initial value of the plume diameter to be a function of the local atmospheric pressure. This pressure, approximated by $p(z) = 1222 \exp(-0.155z)$ mbar (z in km), decreases from 55 mbar at 20 km to 2.5 mbar at 40 km. Zittel [1] finds that the afterburning exhausting gases cool and expand to near-ambient conditions within a few seconds of entering in the stratosphere. He also finds that the radius of the plume is approximately 20 m at an altitude of 20 km in these first few seconds. Since the ambient temperature is constant within 15% throughout the stratosphere, one expects that this initial plume diameter will scale as $p(z)^{-1/2}$, creating an initial radius of about 40 m at an altitude of 20 km and 100 m at 30 km. Then, following Eqs. 3 and 7,

$$K_{yy}(z) = b[R_i(z) + 2bt], \tag{8}$$

where

$$R_i(z) = [p(z_0)/p(z)]^{1/2} R_{i0}\ , \tag{9}$$

where R_{i0} is the initial reference radius of the Titan plume at the nozzle exit plane ($\approx$ 20 m at an altitude of 20 km). This scaling affects the plume diameters only at the earliest times and is negligible at all measurement times.

Table IV

Diffusion Data- Model Comparision

	DATA			**DIFFUSION MODELS**				
Source	**Hoshizaki [19]**	**Strand *et al.* [20]**	**Titan IV K-10**	**Watson *et al.* [22]**	**Denison *et al.* [2]**	**Ross [8]**		
Altitude	18	19	30	alt. indep.	alt. indep.	20	30	40
D (km) at 10 min	3.0	1.5-5	6.0	0.23	4.2	0.5	0.4	0.67
Expansion Rate (km/h)	18	9.-30	36	1.4	25	2.9	2.4	4.0
Chemistry Model using Diffusion Model	Ref. [2]			Ref. [7]	Refs. [2], [4], [7]	Ref. [8]		

Table IV compares the measured and model values. Given the large variability of climate that can affect plume expansion rates, the agreement among the observed values must be considered remarkable. The models show considerably less agreement among their values. The Watson *et al.* model predicts the smallest value for the 10-min diameter. This is not surprising since the model was designed for long times, and the authors speculate that their model may under-predict the initial diameters. The predictions of the Ross model are a factor of two greater than the Watson *et al.* model but are still an order of magnitude below the predictions of the model of Denison *et al.* The model of Denison *et al.* most closely reproduces the observed diameters, which is not surprising given that its diffusion coefficient is based on the Hoshizaki data.

Table IV also indicates the diffusion models used as inputs to the models of stratospheric plume chemistry. Chemical models using the diffusion model of Watson *et al.* will predict chemical concentrations that are too large at early times. The dispersion at long times is best approximated by this model, after the eddy diffusion lengths have reached meteorological scales of hundreds of kilometers. This may require a day or more. The model of Denison *et al.* should be the most accurate at short times and will result in chemical concentrations that are less than those predicted by Refs. [7] and [8]. Since several of the chemical reaction rates depend quadratically on chemical concentration, the chemistry will depend quite severely on this initial expansion rate. Indeed, this dependence has been modeled by Brady and Martin [7], showing that the size and persistence of the ozone hole depend on the dispersion rate, peaking for the rate chosen for their work. Accordingly, the size and persistence of the predicted local ozone depletion by all of the plume chemistry models depend critically on the initial plume dispersion rate. Since all instruments under consideration for verifying ozone chemistry models of the plume are designed to operate in the first 24 hours, they should use models that employ the early plume dispersion rates.

2.4 Model for the Specific Particle Density

Based on the foregoing discussion, we present a model for the specific density of particles (number/air volume/particle diameter) for a Titan IV plume as a function of position and time. In this model, we assume that the particle density is a smoothly varying, cylindrically symmetric function. This is obviously an oversimplification as any visual observation of the expanding plume will show (see for example Appendix II of Ref. [19]). Nevertheless, for the purposes of line-of-sight observations through the plume and measurements or calculations time-averaged over a time interval, this convenient approximation is useful. The radial and temporal dependence is taken from the solution of the conservation equation for a line source and a scale-dependent diffusivity. The functional dependence on the particle diameter is assumed to be exponential following the analysis of the experimental data presented in Figs. 3 and 4. Then for a single particle-size distribution mode we write

$$\begin{aligned} n_D(D,r,z,t) &\equiv \frac{dn(D,r,z,t)}{dD} \\ &= n_{D0}(z)\left(\frac{t_0}{t}\right)^2 \exp[-r/b(z)t]e^{-\gamma D} \end{aligned} \tag{10}$$

where D is the particle diameter, and the time dependence of normalization parameter, $n_0(z)$, is factored out to give $n_0(z)$ the intuitive dimensions of specific density. In general, the parameters $n_0(z)$ and $b(z)$ are altitude dependent. Certainly, the initial value of the plume diameter, and hence its particle density, is a function of the local atmospheric pressure. As noted in Section 2.2.3 this initial diameter is small, about 80 m at an altitude of 20 km and 200 m at 30 km. The line-source solution of the conservation equation assumes a negligible inital plume diameter. Since these diameters are small compared to the observed plume diameters after a minute or two of expansion, this solution is a good approximation after a few minutes and this altitude dependence will be ignored. As discussed above, the altitude variation of the small eddy diffusion coefficient, $b(z)$, is unknown, and the limited evidence currently available suggests that its dependence on altitude is small. Pending better data, we will consider this parameter to be independent of altitude also. As noted in ref. 13, available evidence also suggests that the particle size mode parameter, γ, is independent of altitude.

The particle size distribution is assumed to be trimodal. The small- and medium-size distributions are given by those shown by the fits in Fig. 3. The large particle distribution is given by the intermediate fit values inferred from the curves in Fig. 4, constrained to give the same density value at 1 μm as that of the medium diameter particles in Fig. 3. Generalizing Eq. 10 to an expression for trimodial distribution is done by a straightforward summation of the (assumedly) independent number densities of each distribution. Also as discussed, each mode has a different initial spatial distribution. The small particles (< 0.25 μm) readily follow propellant gas through the rocket nozzle and thus are evenly distributed across the diameter of the plume. Particles greater than 1 μm in diameter do not follow the flow and are confined to the central core of the plume. This segregation affects only the initial radius (and hence density) of the plume and also can be included in the normalization parameter. The expansion rate of the each of the modes, however, will be considered to be equal.

We define the region for averaging the particle density over the assumed exponential spatial distribution to be the radius where the number density falls to e^{-2} of its peak value. This averaging is used to obtain the peak particle number densities for the three modes. The normalization procedure is discussed in Appendix I and it yields:

$$n_D(D,r,t) = \left(\frac{t_c}{t}\right)^2 \exp\left(-\frac{r}{bt}\right)\sum_{i=1}^{3} n_i e^{-\gamma_i D}\ , \tag{11}$$

where

$n_1 = 8.3 \times 10^{12}\ \mathrm{m^{-3}\ \mu m^{-1}}$ $\qquad \gamma_1 = 63.3\ \ (\mu\mathrm{m})$
$n_2 = 1.8 \times 10^{8}\ \mathrm{m^{-3}\ \mu m^{-1}}$ $\qquad \gamma_2 = 3.13\ \ (\mu\mathrm{m})$
$n_3 = 3.3 \times 10^{7}\ \mathrm{m^{-3}\ \mu m^{-1}}$ $\qquad \gamma_3 = 0.80\ \ (\mu\mathrm{m})$

$t_c = 344$ s, and the summation is over the three particle size modes. The particle number density for a given range of particle size is obtained by integrating Eq. 9 over the particle diameter for the range (see Eq. 12 below). This model predicts particle size distribution and density for SRM plumes in the 18-40 km range during its early expansion. It is useful for predicting the effects of particles on data taken by optical instruments designed to measure the physical and chemical properties of the plume in this altitude range.

2.5 Predicted Physical Characteristics of SRM Exhaust Based on Model

The physical properties of the plume due to the particles can be readily calculated using the particle model. The total number density, $n(r,t)$, the total area of all particles per volume of air, a_{tot}, and the mass per volume of air, C_m,, are given, respectively, by:

$$n(r,t) = \int_0^\infty n_D(D,r,t)dD \tag{12}$$

$$a_{tot}(r,t) = \int_0^\infty n_D(D,r,t)A(D)dD \tag{13}$$

$$C_m(r,t) = \int n_D(D,r,t)\rho(D)V(D)dD\ , \tag{14}$$

where $n_D(D,r,t)$ is given by Eq. 11. The surface area of a particle, $A(D) = \pi D^2$, and the volume of a particle, $V(D) = \pi D^3/6$, are assumed to be time independent. As noted above, the particle density varies with particle size. For this, we choose a model of density that varies exponentially with particle diameter, *viz.*,

$$\rho(D) = 1.65 + 2.4 \times 10^{-0.195D} \quad (D \text{ in } \mu\text{m}, \ \rho \text{ in gm/cm}^3). \tag{15}$$

This function yields a density of 1.7 gm/cm^3 at a particle diameter of 10 μm, 4.0 gm/cm^3 at 0.01 μm, and reasonable intermediate values. Eqs. 12-14 can be evaluated separately for each of the three modes. Peak values ($r = 0$) for these quantities at $t = 600$ seconds are shown in Table V. The peak values can be converted to values spatially averaged over a diameter defined by the distance required for the number density to drop to e^{-2} of its peak value by multiplying the peak value by 0.43 (see Appendix I).

Table V
Plume-Particle Characteristics from Model

Particle Mode	Sauter Mean Diameter D_{32} (μm)	Average Particle Density ρ_{avg} (gm/cm^3)	Mass Fraction in Particle Model	C_m Mass per Volume Air: Peak Value (gm/cm^3)	Number Density: Peak Value (cm^{-3})	Total Particle Area per Volume Air: Peak Value (μm^2/cm^3)
Small	0.056	4.0	0.012	2.0×10^{-12}	8.8×10^{3}	53
Medium	1.0	3.6	0.015	2.4×10^{-12}	7.94	6.7
Large	3.6	2.6	0.974	1.6×10^{-10}	6.16	125

Examination of Table V shows that nearly all the mass is in the large particles, but the small particle number density is much greater than the number density of large particles, as expected. The total surface area available for the heterogeneous reactions resides mostly in the large particles even though the small particles offer much greater surface area on a per mass basis. Since both the small- and large-mode particles contribute comparable surface areas, this area should be measured for both modes. As shown below, the large particle surface area is more amenable to measurement by transmission techniques because it has a large attenuation coefficient.

Caution must be exercised when calculating size properties (diameter, surface area, volume, mass, etc.) using exponential particle size distributions. Physical distributions are not exponential on the low and high ends of the size parameter. Mugele and Evens [46] show that fitting exponential functions to size histograms can predict erroneous size properties if the distributions are not properly truncated. They introduce an upper-limit distribution function (ULDF) that limits the largest particle size to a specified finite diameter. The ULDF is written in terms of two additional parameters that do not lend themselves to direct geometrical interpretations. (See, for example, Dobbins *et al.* [47].) There are only four data points in each of the two modes in Fig. 3, and fitting a three parameter ULDF to these few points does not yield well-defined parameters. Accordingly, it was decided to keep the exponential fits shown in Figs. 3 and 4 and set the limits of integration to the values of the smallest and largest diameters measured.

Decreasing the lower limit of integration to zero in the small mode increases the area percentage in this mode by about 5%. Increasing the large mode integration limit to 100 μm increases the large mode area percentage by about 1%. The fits shown in Fig. 3 are to the most complete data sets given in ref. 19 (Fig 13 ref. 27, t = 13 min.). A less complete data set also given in this reference (Fig. 12 ref. 27 , t= 7 min.) has a smaller exponent and puts a somewhat greater fraction of the surface area in the small particle mode.

3.0. Optical Measurements in the Plume

3.1 Transmission

The transmission, T, of radiation through a uniform medium of length, L, containing particles of uniform number density, n, and equal geometrical cross sectional area, a, is given by Bouguer's law:

$$T = \exp(-QanL) = \exp[-(3QC_mL/2\rho D)], \tag{16}$$

where Q is the scattering efficiency, C_m is the mass concentration of the particles in the medium (gm cm^{-3} of air), ρ is the mass density of a particle, and D is the diameter of the particles. If the particles are not of uniform size (polydisperse systems), the transmission can be written in terms of mean parameters [48]:

$$T = \exp[-(3\,\bar{Q}C_mL/2\rho D_{32})] \;\equiv\; \exp[-\beta_{avg}L], \tag{17}$$

where β_{avg} is the attenuation coefficient, D_{32} is the volume-weighted-to-area-weighted (Sauter) mean diameter

$$D_{32} \equiv \frac{\int_0^\infty n_D(D)D^3dD}{\int_0^\infty n_D(D)D^2dD}, \tag{18}$$

and $\bar{Q}$ is the efficiency averaged over the distribution function:

$$\bar{Q} = \frac{\int_0^\infty n_D(D)Q(\alpha(D), p+iq)D^2dD}{\int_0^\infty n_D(D)D^2dD}. \tag{19}$$

Here, α is the size parameter ($= \pi D/\lambda$), and $p+iq$ is the complex index of refraction of the particles. The scattering efficiency, Q, can be calculated for spherical particles for any values of α, p, and q using Mie scattering theory (see below). The power of this representation is that for a dispersion of particles, $\bar{Q}$ depends primarily on the mean diameter, D_{32}, and is independent of the shape of the size distribution function for a monomodal distribution. Furthermore, for the case of small absorption (small imaginary component of the index of refraction), the ratio of $\bar{Q}(\lambda_1)/\bar{Q}(\lambda_2)$ is montonic as a function of D_{32} for $\lambda_1/3 < D_{32} < \lambda_2$. Therefore, a

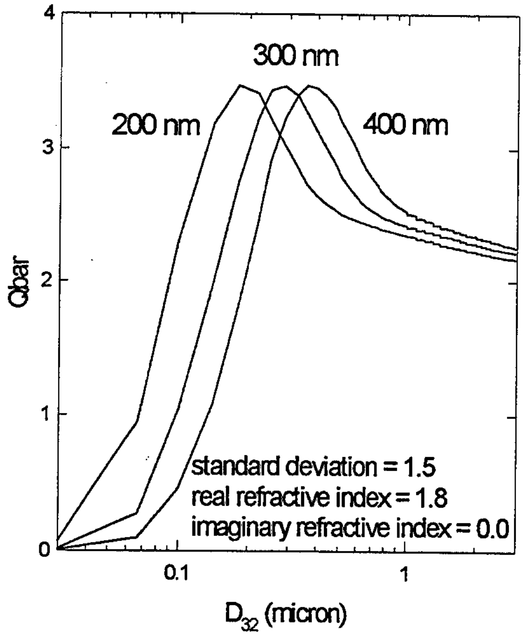

Figure 8. Calculated mean efficiency factors as a function of D₃₂ for near-ultraviolet wavelengths.

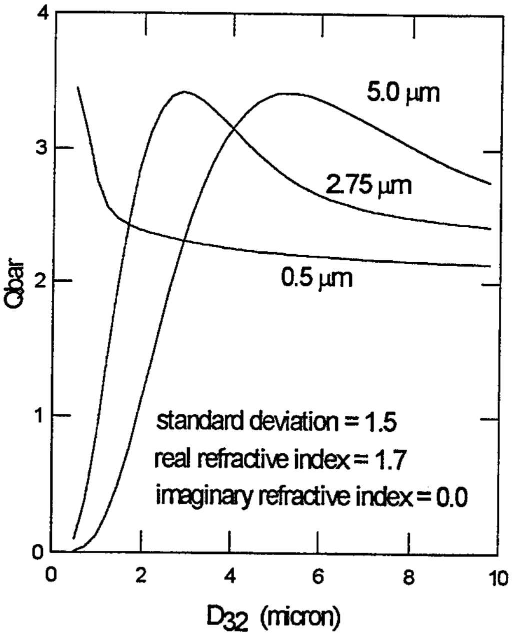

Figure 9. Calculated mean efficiency factors as a function of D₃₂ for visible and infrared wavelengths.

measure of the transmittance at two wavelengths will allow the Sauter mean diameter to be determined as discussed below.

3.2 Mie Scattering Calculations

In order to predict the transmission characteristics of the SRM plume, Mie scattering theory was used to calculated the mean scattering efficiency. Mie is a rigorous application of Maxwell's equations to the problem of the scattering of electromagnetic waves by spheres of arbitrary size. Classic works that describe Mie theory are by Kerker[49] and by van de Hulst[50]. The results of the calculations presented here were obtained using a FORTRAN code [51] that was modified for this work to give a greater range of particle sizes and to produce spectral output. This code permits the calculation of the mean value of the scattering efficiency for a distribution of particles sizes. The code uses a log-normal distribution for the particle sizes, but, as noted above, the mean values of the scattering efficiency are insensitive to the shape of the distribution function. This is true only for monomodal particle size distributions, which is not the case in this (trimodal) application. However, if the attenuation is negligible for all but one mode, then the distribution may be considered to be monomodal. This is shown to be the case for the SRM plume.

Figures 8 and 9 show calculated mean efficiencies as a function of D_{32} for a monomodal log-normal dispersion distribution with a standard deviation of 1.5 and an assumed imaginary refractive index of zero. Fig. 8 uses a real refractive index of 1.8, which is characteristic of rocket plume alumina particles for wavelengths of 200, 300, and 400 nm. Figure 9 shows a similar calculation for wavelengths of 0.5, 2.75, and 5.0 μm. A real index of refraction of 1.7 was assumed for these visible and infrared wavelengths. The scattering efficiency is greatest when the mean particle diameter is approximately equal to the wavelength of light. At much smaller diameters, the efficiency approaches small values that can be calculated using Rayleigh theory, whereas at larger diameters the efficiency approaches a value of two. The mean scattering efficiencies for selected wavelengths of interest for each of the three particle size modes expected in the plume are given in Table VI.

Table VI
Scattering Efficiencies

Mode	**D_{32} (μm)**	**Mean Scattering Efficiency ($\bar{Q}$)**					
		$\lambda = 0.2\mu m$	0.3μm	0.4μm	0.5μm.	1.0μm	5.0μm
Small	0.056	0.7	0.18	0.058	1.5×10^{-2}	1.6×10^{-5}	1.5×10^{-6}
Medium	1.0	2.35	2.42	2.52	2.74	0.90	0.13
Large	3.6	2.15	2.19	2.22	2.3	2.9	3.3

4.0 Applications

In this section, we consider three applications of the particle model and the optical scattering results presented in the previous sections. The first is the calculation of the local attenuation spectrum seen by a transmission instrument traversing the plume by aircraft in the stratosphere. This information is required to project the feasibility of measuring the chemical concentration of species in the plume using direct optical absorption in the ultraviolet spectral region. The second is an ingeniously simple method of measuring the specific density of total particle surface area using a two-wavelength transmissometer. This parameter together with the reactive sticking coefficient can be used to discover the effect of heterogeneous chemical reactions in the plume. The third is the measure of the transmission across the plume at an arbitrary angle. This information is useful for estimating the feasibility of plume LIDAR measurements.

4.1 Extinction Spectra in Plume

Verification of the complex computer codes used to model the stratospheric chemistry in an SRM plume is one of the principal goals of the observational work under consideration. Most major chemical species of interest in the plume absorb radiation in the 200 - 400 nm spectral region. Thus it may be possible to measure these chemical concentrations by direct absorption if attenuation from particles is small compared to the molecular absorptions.

The mean scattering efficiencies as a function of wavelength in this spectral region were calculated using Mie theory for three Sauter mean diameters. The D_{32} values chosen for the calculation are those of the predicted trimodal particle size distribution given in Section 2.2. The results of these calculations are shown in Fig. 10. The efficiency factors for the small particles ($D_{32} = 0.056\mu m$, bottom of Fig. 10) are small for all wavelengths in this spectral range. The medium- and large-particle distribution scattering efficiencies are appreciative at all these wavelengths.

The mean scattering cross section, $\overline{QA}$, will be large for the large particles in this wavelength interval, but the number densities will favor the small-particle attenuation coefficients. To compare the attentuations due to the molecular absorption and the particle scattering, the attentuation coefficient must be computed. The scattering attenuation coefficients are a product of the particle loading, scattering efficiencies, and the geometrical sizes of the particles, *i.e.* from Eq. 17

$$\beta_{avg}(\lambda)_i = \frac{3\overline{Q}(\lambda)_i (C_m)_i}{2(\rho_{avg})_i (D_{32})_i}, \tag{20}$$

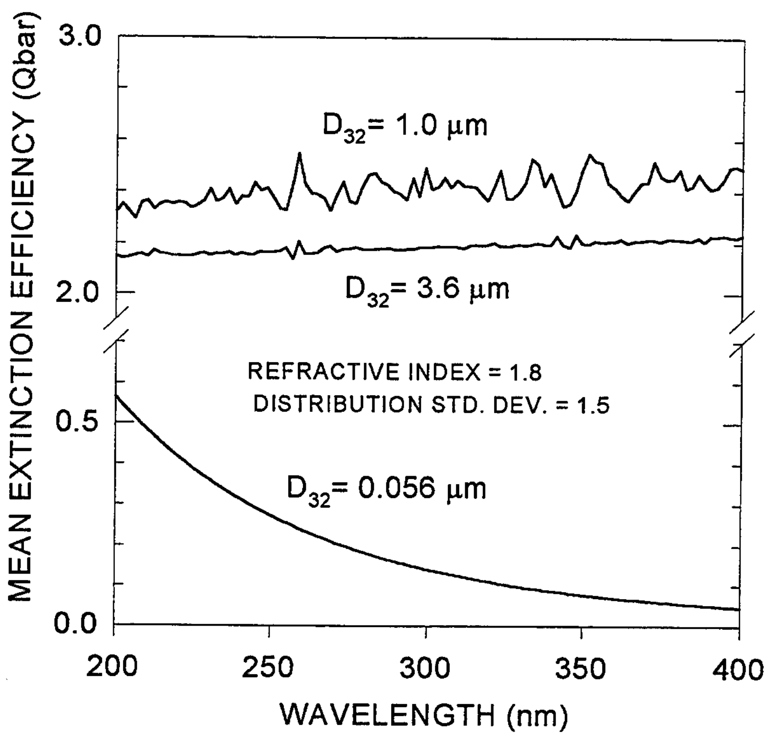

Figure 10. Efficiency factors for three distributions as a function of wavelength.

where $\overline{Q}$ is defined by Eq. 19, ρ_{avg} is averaged over the mode of the particle size distribution (see Table V), and the subscript i (= 1 - 3) is the index of the particle size mode. Using the mean efficiencies from Fig. 10, Eqs. 14 and 15 and the particle model given by Eq. 11, the peak (r = 0) attenuation coefficients due to particle scattering are calculated for three times and are presented in Fig. 11.

These curves indicate that nearly all the optical attenuation in this spectral region is due to the large particles. The advantage of the large number density of the small particle distribution is outweighed by the large values of scattering efficiencies and the geometrical cross sections of the large particles. Thus for the purposes of optical measurements in the plume in this near-ultraviolet spectral interval, the particles size distribution may be considered to be monomodal, and inference of Sauter mean diameter from particle attenuation measurements at two or more wavelengths will correctly yield the D_{32} values for the large-mode distribution. The values of this attenuation can be compared to the molecular absorbances obtained from the known molecular absorption cross sections and the species concentrations calculated from the chemical models at the corresponding times.

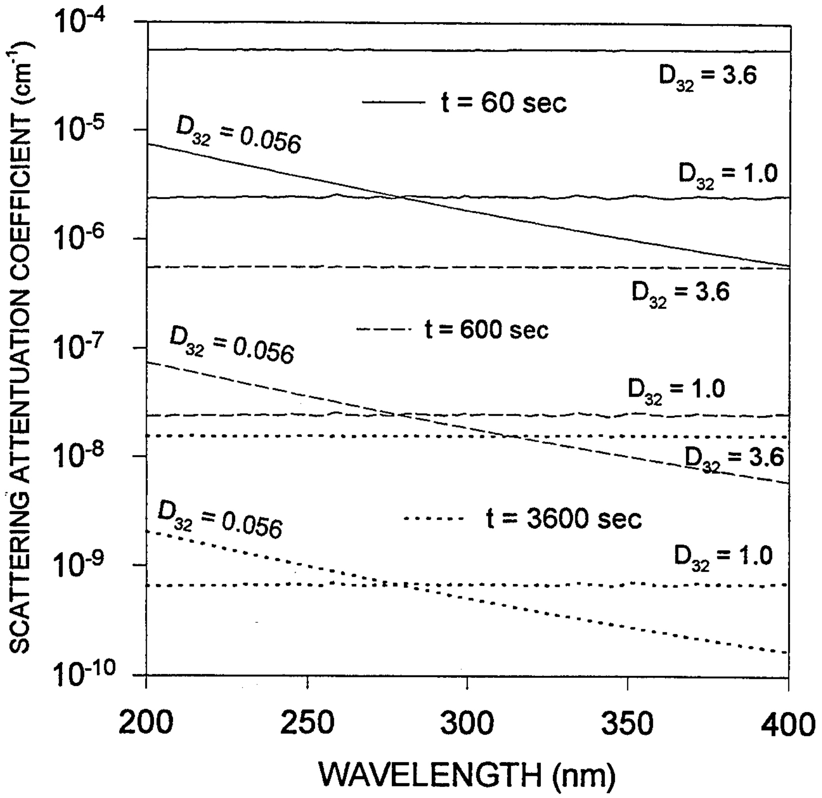

Figure 11. Attenuation coefficients using particle-plume model at times of 1 min., 10 min., and 1h. after SRM passage.

4.2 Measurement of Total Particle Surface Area per Air Volume

In this subsection, it is shown that the total particle surface area in the plume per unit gas volume is inversely proportional to the Sauter mean diameter of the particles--a parameter easily measured by a transmissometer. Accordingly, this required parameter for gauging the effect of heterogeneous chemistry can be measured without approximation using a relatively simple optical instrument. The curves required to infer the Sauter mean diameter from the measured transmissions are calculated using Mie scattering theory.

4.2.1 Relationship between Specific Total Particle Surface Area and Average Particle Size

If all the particles in the plume have the same size, the total surface area of the particles per unit gas volume is simply the total number of particles per volume times the surface area per particle. For a particle size distribution, the total area per gas volume is obtained from Eq. 13:

$$a_{tot} = \pi \int_0^\infty n_D(D) D^2 dD . \qquad (21)$$

Similarly, the total volume of particles per unit gas volume is:

$$v_{tot} = \int_0^\infty n_D(D)V(D)dD = \frac{\pi}{6}\int_0^\infty n_D(D)D^3 dD. \tag{22}$$

Now, we note that

$$\frac{a_{tot}}{v_{tot}} = \frac{6}{D_{32}}, \tag{23}$$

where Eq. 18 was used for D_{32}. Furthermore, we note that $v_{tot} = M_L/A_p\rho_{avg}$ where M_L is the mass of the alumina particles ejected per vehicle track length, A_p is the cross-sectional area of the plume, and ρ_{avg} is the average density of the particles. Substituting this expression for v_{tot} in Eq. 4, we obtain

$$a_{tot} = \frac{6M_L}{A_p\rho_{ave}D_{32}}. \tag{24}$$

Eq. 24 is an important result because it shows how the volume density of the total particle surface area can be obtained from known or easily measured quantities. The mass of the alumina per vehicle track length is 15.0 gm/cm for a Titan IV at 20 km, the cross-sectional area of the plume is measured on traversal of the plume, and the average density of the particles is approximately 3.0 gm/cm^3 (see Table V). As discussed in the next section, the Sauter mean diameter, D_{32}, is readily measured using the transmission of light at two wavelengths.

4.2.2 Measurement of the Sauter Mean Diameter by a Two-Color Transmissometer

Inspection of Eq. 17 shows that the ratio of measurements of transmission at two wavelengths can be expressed as a simple function of the mean efficiency of a distribution with a given D_{32}.

$$f(D_{32}) = \frac{\overline{Q_2(D_{32})}}{\overline{Q_1(D_{32})}} = \frac{\ln[T(\lambda_2)]}{\ln[T(\lambda_1)]} \tag{25}$$

This function can be calculated for the wavelengths and refractive index of the particles using Mie scattering theory. This was done for three wavelengths in the visible and infrared spectral regions where the attenuation is larger than in the ultraviolet region. The results are shown in Fig. 12. For the case of small absorption (small imaginary component of the index of refraction), this function is monotonic for $\lambda_1/3 < D_{32} < \lambda_2$. Accordingly, the value of D_{32} can be inferred from one of these curves given the measured transmissions for a monomodal distribution. As noted above, the attenuation due to the large-particle distribution is considerably greater than that of the small- and medium-particle distributions due to their geometrical size and scattering efficiencies (see Table VI). Thus the distribution will appear to be monomodal, and only the Sauter mean diameter of the large mode will be measured. Although the largest region of monotonicity is given by the ratio $\bar{Q}(D_{32}, \lambda=0.5\ \mu m)/\ \bar{Q}(D_{32}, \lambda=5.0\ \mu m)$, the ratio $\bar{Q}(D_{32}, \lambda=2.75\ \mu m)/\ \bar{Q}(D_{32}, \lambda=5.0\ \mu m)$ is the better ratio to use for this application because: 1) the attenuation coefficient at 2.75 µm is greater for the large mode particles; 2) the at-

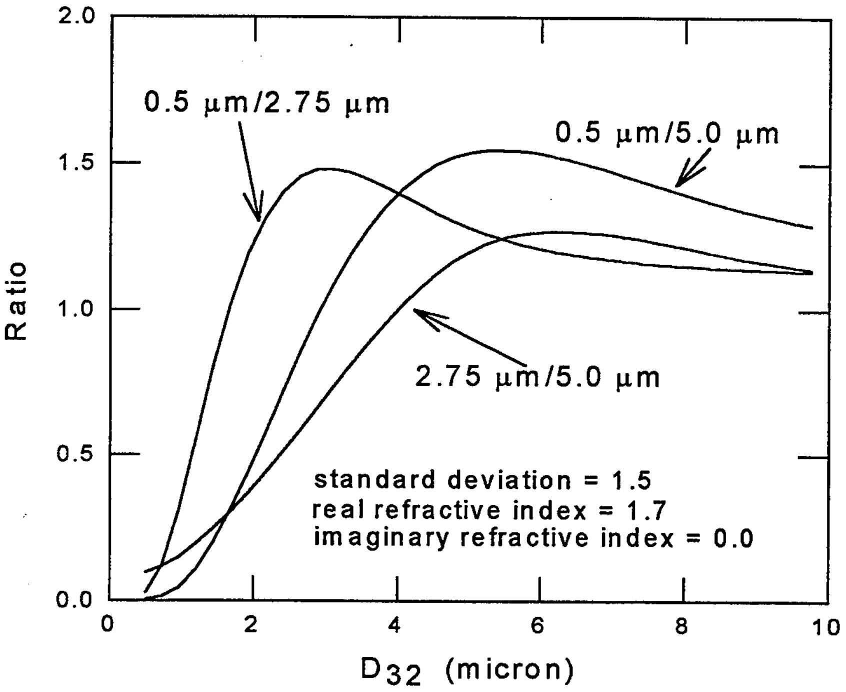

Figure. 12 Ratio of the mean scattering efficiencies (see Eq. 25) for three wavelength calculated using Mie theory for three wavelengths shown in Fig. 6. Locating the ratio of the log of the measured transmission at two wavelengths on the ordinate of the function allow the Sauter mean diameter D_{32} to be inferred from the abscissa.

tenuation is smaller for the medium mode particles better approximating a monomodal distribution; and 3) the expected mean diameter lies near the center of the region of monotonicity .

Only one of the curves shown in Fig. 12 is required to measure D_{32} if the value of the width w of the distribution and the complex refractive index are known. If these quantities are not known, several transmission measurements can be taken at different wavelengths. The ratios of these measurements can then be compared with the calculated curves of ratios of $\bar{Q}(D_{32})$ vs. D_{32}. If $\bar{Q}(D_{32})$ was calculated for the correct size distribution width and index of refraction, then all the measured ratios will yield identical values of D_{32}. Alternatively, a multiparameter fit of the of the calculated values of $\bar{Q}(D_{32}, w, p+iq)$ to the measured ratios will allow the determination of D_{32}, w, and $p+iq$. In practice, the value of the imaginary part of the refractive index (q) is small for alumina particles at wavelengths below 6.5 µm [52] and may be ignored, leaving only three parameters to fit. For example, Kim *et al.* [24] used transmissions at five wavelengths to determine the Sauter mean particle diameter (0.150 µm ± 8%), standard deviation (1.50 ± 3%) and real index of refraction (1.63 ± 8% for visible wavelengths) of the particles at the edge of a plume from a small solid-propellant motor.

4.3 Transmission across the Plume at Arbitrary Angle

Generalizing Eq. 17 to a spatially nonuniform distribution of particles, the transmission of a beam of light crossing the centerline of a plume and making an angle θ with respect to its axis (see Fig. 13) is given by

$$T = \exp\left[-\int \beta_i(t,\ell)\,d\ell\right], \tag{25}$$

or using Eq. 20

$$T = \exp\left[-\kappa_i \int_{-r}^{r} C_m(r,t)\,dr\right], \tag{26}$$

where the attenuation parameter is

$$\kappa_i = \frac{3\overline{Q_i(\lambda)}}{2\rho(D_{32i})D_{32i}\cos\theta}, \tag{27}$$

i is the index for the particle size mode, and C_m is given by Eq. 14. Using the mean efficiencies from Table VI and angle of 45° (an appropriate value assuming a vertical LIDAR beam and a typical trajectory of a Titan IV in the stratosphere), transmissions through the plume at three wavelengths for each of the three particle modes are given in Table VII for a time of ten minutes after SRM passage. Again, nearly all the attenuation is due to the large particles. The time dependence of the transmission for the large mode particle at a wavelength of 300 nm is show in Fig. 14. The plume becomes more than 50% transparent in the first five minutes.

Table VII
Plume Transmissions at 45°

Mode	D_{32} (μm)	Transmission		
		$\lambda = 0.2\mu m$	$0.3\mu m$	$5.0\mu m$
Small	0.056	0.964	0.991	1.000
Medium	1.0	0.989	0.989	0.999
Large	3.6	0.761	0.757	0.657

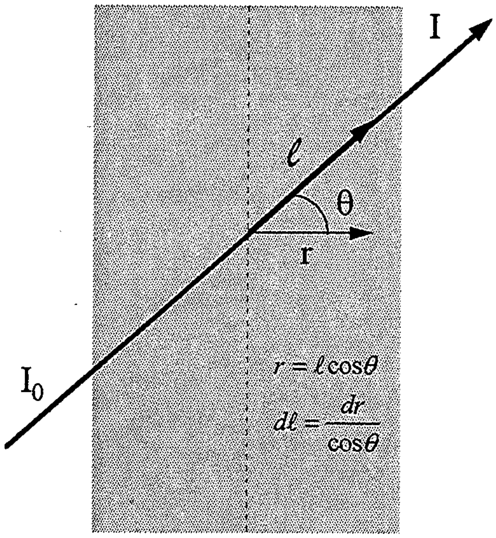

Figure 13. Geometry of the attenuation of a beam of light traversing a plume at an arbitrary angle.

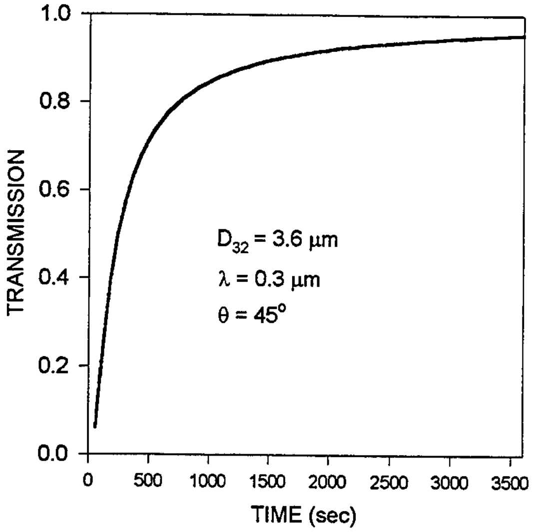

Figure 14. Transmission of beam of radiation across plume as a function of time after the passage of the SRM.

5.0 Summary and Conclusions

This report presents a unified model for the particle size distribution, particle density, and geometrical dispersion for the alumina particles in the exhaust of a Titan SRM plume in the stratosphere. This model is based on what is believed to be the best available data. However, there are serious gaps in the data base, especially in the dispersion rates of the plume after the first 10 min. The particle size distribution is found to be trimodal with nearly all the particles in the small-size mode but with nearly all the mass in the large-size mode. About two-thirds of the particle surface area available for heterogeneous chemical reactions is due to the large particle mode while most of the remaining surface area is due to the small particle mode. The light scattering characteristics of the plume were also explored based on the model. Mie scattering calculations where used to predict the local attenuation of the plume as a function of wavelength. Mie theory was also used to calculate the total attenuation of a beam of radiation passing through the plume making an arbitrary angle with respect to the axis of the plume and as a function of time after SRM passage for several wavelengths in ultraviolet, visible, and infrared spectral regions. These studies show that most of the attenuation is due to the large-size mode and for the purposes of light scattering, the plume may be considered monomodal with a Sauter mean diameter of 3.6 μm. Additionally, a simple relationship for the volume density of total area of the particles was derived in terms of known parameters and the Sauter mean diameter. Subsequently, it was shown that the Sauter mean diameter of the large-size mode could be measured using a two-color transmissometer. These results will be useful for designing instruments required to measure the chemical and physical properties of the SRM plume and predicting the effect of such a plume on the stratospheric ozone chemistry.

6.0 References

1. P.F. Zittel, "Local effects of large, solid rocket motors on stratospheric ozone" The Aerospace Corporation ATR-92(9558)-2; "Computer model predictions of the local effects of large, solid-fuel rocket motors on stratospheric ozone," The Aerospace Corporation TR-94(4231)-9

2. M.R. Denison, J. J. Lamb, W. D. Bjorndahl, E. Y. Wong, and P. D. Lohn, "Solid rocket exhaust in the stratosphere: Plume diffusion and chemical reactions," AIAA 92-3399, July, 1992: also in *J. Spacecraft &Rockets* **31**, 435-442 (1994).

3. B.C. Kruger, M. M. Hirschberg, and P. Fabian, "Effect of solid-fueled rocket exhausts on the stratospheric ozone layer," *Ber. Bunsenges. Phys. Chem.* **96**, 268-272 (1992).

4. B.C. Kruger, "Ozone depletion in the plume of a solid-fuel rocket," *Ann. Geophysicae* **12**, 409-416 (1995).

5. R.B.Cohen, "Estimating the relative ozone-removing efficiency of launch vehicle chlorine effluent," Aerospace Corporation Internal Study (1993) [ATM 94(8446)-1].

6. L.R. Martin, "Possible effect of the chlorine oxide dimer on transient ozone loss in rocket plumes," The Aerospace Corporation TR-94(4231)-1 (15 March 1994).

7. B.B. Brady and L. R. Martin, "Modeling solid rocket booster exhaust plumes in the stratosphere with SURFACE CHEMKIN," The Aerospace Corporation, TR-95(5231)-9 (1995)

8. M. Ross, "Local Impact of Large Solid Rocket Motor Exhaust on the Stratospheric Ozone and Surface Ultraviolet Flux," *J. Spacecraft & Rockets*, in press (1995).

9. H.S. Pergament, R. I. Gomberg, and I. G. Poppoff, "NO_x deposition in the stratosphere from the space shuttle rocket motors," Appendix G to *NASA Tech. Memo. Z-58198*, G-3, Han 1977.

10. E.J. Beiting, "Optical measurements in a Titan rocket plume in the stratosphere," Aerospace Corporation Internal Study (1993) [ATM-94(4566-03)-1].

11 . J.A. Gelbwachs, "Lidar monitoring of SRM exhaust particles in the stratosphere," Aerospace Corporation Internal Study, (1993) [ATM-94 (4488)-2].

12. E.J. Beiting, "In-situ stratospheric ultraviolet absorption and extinction measurements in a Titan IV plume," Aerospace Corporation Internal Study, (1994) [ATM-94(4448-7)-1].

13. E.J. Beiting, "In-situ stratospheric measurement of total particle surface area in SRM plumes by optical transmissometer," Aerospace Corporation Internal Study (1994) [ATM-94(4232-05)-1].

14. J.A. Syage, "Airborne differential absorption lidar (DIAL) monitoring of ozone in a solid rocket motor plume," Aerospace Corporation Internal Study (1994) [ATM-94(4448)-6].

15. R.B. Cohen, J. A. Syage, L. R. Martin, B. B. Brady, E. J. Beiting, A. McIlroy, and S. T. Amimoto, "Understanding the effect of solid rocket propellant exhaust on stratospheric ozone depletion," Aerospace Corporation Internal Study (1994) [ATM 94(4231-16)-3].

16. J.A. Syage, "Can TOMS measure ozone depletion in rocket plumes?," The Aerospace Corporation, TR-95(5231)-4 (15 Jan 1995).

17. J.A. Syage, "Direct absorption spectroscopy of a solid rocket plume," The Aerospace Corporation, TOR-95(5231)-1 (15 April 1995).

18. D.L. McKenzie *et al.*, "System requirements for the high-resolution ozone imager (HIROIG)," The Aerospace Corporation, TR-93(3231)-2 (15 September 1993).

19. E.J. Beiting, "Solid Rocket Motor Statospheric Plume Dispersion," Aerospace Corporation Internal Study (1995) [ATM-95(5631-16)-3].

20. M. E. Zolensky, D. S. McKay, and L. A. Kaczor, "A tenfold increase in the abundance of large soliid particles in the stratosphere, as measured over the period 1976-*1984," J. Geophys. Res.* **94**, 1047-1056 (1989).

21. E.D. Youngborg, T.E. Pruitt, M.J. Smith, and D. W. Netzer, "Light-diffraction particle size measurements in small solid-propellant rockets," *J. Propul. Power* **26**, 243-249 (1990)

22. W. D. Brennan, D. L. Hovland, and D. W. Netzer, "Measured particulate behavior in a subscale solid propellant rocket motor," *J. Propul. Power* **26**, 243-249 (1990)

23. D. Laredo and D. W. Netzer, "The dominant effect of alumina on nearfield plume radiation," *J. Quant. Spectrosc. Radiat. Transfer* **50**, 511-530 (1993).

24. H. O. Kim, D. Laredo, and D. W. Netzer, "Measurement of submicrometer Al_2O_3 particle in plumes," *Appl. Opt.* **32**, 6834-6840 (1993).

25. D. Laredo, J. C. McCrorie II, J. K. Vaughn, and C. W. Netzer, "Motor and plume particle size measurements in solid propellant micromoters," *J. Propulsion Power,* **10**, 410-418 (1994).

26. L. F. Radke, P. V. Hobbs, and D. A. Hegg, "Aerosols and trace tases in the effluents produced by the launch of large liquid- and solid-fueled rockets," *J. of Appl. Meteorology*, **21**, 1312-1345 (1982).

27. L. D. Strand, J. M. Bowyer, G. Varsi, E. G. Laue, and R. Gauldin, "Characteristics of particles in the exhaust plume of large solid-propellant rockets," *J. Spacecraft,* **18** (4), 297-305 (1981)

28. W.R. Cofer, III, G.C. Purgold, R.A. Edahl, and E.L. Winstead "Solid propellant exhausted aluminum oxide and hydrogen chloride: environmental considerations," AIAA 93-0305, 31st Aerospace Sciences Meeting, Reno NV (1993).

29. W.R. Cofer, III, R.J. Bendura, D.I. Sebacher, G.L. Pellett, G.L. Gregory and G.L. Maddrea, "Airborne measurements of space shuttle exhaust constituents," *AIAA J.*, **23,** 283-287 (1985).

30. W.R. Cofer, III, G.G. Lala, and J.P. Wightman, "Analysis of mid-tropospheric space shuttle exhausted aluminum oxide particles," *Atmos. Environ.* **21,** 1187-1196 (1987).

31. W.R. Cofer, III, G.C. Purgold, E.L. Winstead, and R.A. Edahl, "Space shuttle exhausted aluminum oxide," *J. Geophys. Res.* **96,** 17, 371-17,376 (1991).

32. W.R. Cofer, III, E.L. Winstead, and L.E. Key, "Surface composition of solid-rocket exhausted aluminum oxide particles," *J. Propulsion,* **5**, 674-677 (1989).

33. K. M. Dill, R. A. Reed, V. S. Calia, and R. J. Schultz, "Analysis of crystalline phase aluminum oxide particles from solid propellant exhausts," *J. Propulsion Power*, **6**, 688-671 (1990).

34. R.P. Turco, O. B. Toon, R. C. Whitten, and R. J. Cicerone, "Space shuttle ice nuclei,". *Nature* **298,** 26 August 1982.

35. R.P. Turco, O. B. Toon, J.B. Pollark, R. C. Whitten I. G. Poppoff, and P. Hamill, "Stratospheric aerosol modification by supersonic transport and space shuttle operations--climate implications," *J.Appl. Meteor.* **19,** 78-89 (1980).

36. R. A. Dobbins and L. D. Strand, "A comparison of two methods of measuring particle size of Al_2O_3 produced by a small rocket motor," *AIAA J.* **8**, 1544-1550 (1970).

37. C. J. Hwang and G. C. Chang, "Numerical study of gas-particle flow in a solid rocket nozzle," *AIAA. J* **26,** 682-689 (1988).

38. S.M. Dash, "Analysis of exhaust plumes and their interaction with missile airframes," in *Tactical Missile Aerodynamics,* M. J. Hemsch and J. N. Nielsen, eds., Vol. **104** of *AIAA* Progress in Astronautics and Aeronautics (American Institute of Aeronautics and Astronautics, Inc., New York, N.Y. 778-851 (1986).

39. H. Hoshizaki (Chairman), "Aircraft wake microscale phenomena," Chap 2, pp 60-73, in *The Stratosphere Perturbed by Propulsion Effluents*, edited by G. D. Robinson, H. Hidalgo, and N. Sundararaman (1975). Volume 4 of the CIAP monograph series. U.S. Department of Transportation Rept. No. DOT-TST-75-53. (Available for NTIS as PB249684).

40. J.T. Knudson, K. C. Herr , and R.F. Heidner III, "IR ground based monitoring of launches," briefing for the FY94 Pollution Prevention Program, July 29, 1994. The visible video tape was taken for this work.

41. R.T. Watson, P. E. Smokler, W. B. DeMore, "An assessment of an F_2 or N_2O_4 atmospheric injection from an aborted space shuttle mission," NASA JPL Publication 77-81 (1978).

42. E. Bauer, "Introduction and Overview: The Stratosphere in its Application to CIAP," in *CIAP Monograph 1*, The National Stratosphere of 1974, DOT-TST-75-51, Department of Transportation , Washington, D.C., 1975

43. J.F. Louis, "Two-Dimensional Transport Model of the Atmosphere," Thesis, Universtiy of Colorado, Boulder, Colorado, 1974.

44. F.S. Rowland and M. J. Molina, "Chlorofluoromethanes in the Environment," *Rev. Geophys. space Phys.* **13**, 1-35 (1975).

45. D. Randerson, "Temporal change in the horizontal diffusion parameter of a single nuclear debris cloud," *J. Appl. Meteorology* **11**, 670-673 (1972).

46. R. A. Mugele and H. D. Evans, "Droplet size distributions in sprays," *Ind. Eng. Chem.* **43**, 1317-1324 (1951).

47. R. A. Dobbins, L. Crocco, and I. Glassman, "Measurement of mean particle sizes in sprays from diffractively scattered light," *AIAA J.* **1**, 1882-1886 (1963).

48. R. A. Dobbins and G. S. Jizmagian, "Optical scattering cross sections for polydispersions of dielectric spheres," *J. Opt. Soc. Am.* **56** 1345-1350 (1966).

49. M. Kerker, *The Scattering of Light*, Academic Press, New York, (1969).

50. H. C. Van de Hulst, *Light Scattering by Small Particles*, Dover Publications Inc, New York, 1981 (originally, Wiley, New York, 1957).

51. K. L. Cashdollar, C. K. Lee, and J. M. Singer, "Three-wavelength light transmission technique to measure smoke particle size and concentration," *Appl. Opt.* **18**, 1763-1769 (1979).

52. R.A. Nyquist and R.O. Kagel, *Infrared Spectra of Inorganic Compounds (3800-45 cm^{-1})*, Academic Press, New York (1971).

Appendix I

Normalization of the Particle Density Distribution

The spatial and temporal development of the density is based on the line solution of the conservation equation with a size-dependent diffusion parameter. The functional form can be expressed in the form given by Eq. (11). To normalize, the size distribution is first converted to a density:

$$n(r,z,t) = \int_{D_{\min}}^{D_{\max}} n_D(D,r,z,t)dD$$

$$= \left(\frac{t_c}{t}\right)^2 e^{\frac{r_c}{bt_c}} \sum_{i=1}^{3} a_i n_i \exp\left[-\frac{r_i(t,z)}{bt}\right],$$

where coefficients a_i's are obtained from the integration over the particle size distributions,

$$a_1 = \int_{0.025}^{0.244} e^{-b_1 D} dD \ = 3.21 \times 10^{-3}$$

$$a_2 = \int_{0.245}^{0.99} e^{-b_2 D} dD \ = \ 0.134$$

$$a_3 = \int_{1.0}^{10} e^{-b_3 D} dD \ = \ 0.568$$

Then this spatial distribution is averaged and set equal to the average density measured by Strand *et al.* [20],:

$$\overline{n(z,t)} = \left(\frac{t_c}{t}\right)^2 e^{\frac{r_c}{bt_c}} \sum_{i=1}^{3} n_i \overline{\exp\left[-\frac{r_i(t,z)}{bt}\right]} a_i$$

$$\overline{n(z,t)} = c \left(\frac{t_c}{t}\right)^2 e^{\frac{r_c}{bt_c}} \sum_{i=1}^{3} n_i \ a_i$$

where $\overline{n(z = 19\,km, t = 344\,s)} = 1.14 \times 10^{10}\ m^{-3}$ (converting from a Titan IIIc to a Titan IV density) and c = 0.43 for an average over a radius were the density drops to e^{-2} of its peak value. Finally, setting $z_c = 19$ km, $t_c = 344$ s, $r_c = 2$ km, $b = 1.75$ m/s, and noting $n_1/n_2 = 4.65 \times 10^4$ and $n_2/n_3 = 10.3$ [], we find:

$$n_1 = 0.16$$
$$n_2 = 3.5 \times 10^{-6}$$
$$n_3 = 3.3 \times 10^{-7}$$

It should be noted that the absolute density of this model relies on the density measurement of Strand *et al* [20]. This measurement was made using an electrical mobility analyzers (EMAs). The EMAs were calibrated against a standard at the factory and corrected for operation in the low-pressure operation in the instrument bay of the ER-2. The EMAs measured the densities in the range of 0.03 µm to 1 µm and give absolute concentrations when the sampling time is shorter than the transit time through the plume. Three to eight seconds were required to fill the EMA sample bag and five to ten seconds were required to traverse the early contrail. Thus the EMA could underestimate the density by mixing air from outside the plume into the same volume. Whether this was taken into consideration by these workers in the values reported is not known, but the value of $10^4\ cm^{-3}$ is the highest value they reported, and they stated that this value was consistent with predicted values.

TECHNOLOGY OPERATIONS

The Aerospace Corporation functions as an "architect-engineer" for national security programs, specializing in advanced military space systems. The Corporation's Technology Operations supports the effective and timely development and operation of national security systems through scientific research and the application of advanced technology. Vital to the success of the Corporation is the technical staff's wide-ranging expertise and its ability to stay abreast of new technological developments and program support issues associated with rapidly evolving space systems. Contributing capabilities are provided by these individual Technology Centers:

Electronics Technology Center: Microelectronics, VLSI reliability, failure analysis, solid-state device physics, compound semiconductors, radiation effects, infrared and CCD detector devices, Micro-Electro-Mechanical Systems (MEMS), and data storage and display technologies; lasers and electro-optics, solid state laser design, micro-optics, optical communications, and fiber optic sensors; atomic frequency standards, applied laser spectroscopy, laser chemistry, atmospheric propagation and beam control, LIDAR/LADAR remote sensing; solar cell and array testing and evaluation, battery electrochemistry, battery testing and evaluation.

Mechanics and Materials Technology Center: Evaluation and characterization of new materials: metals, alloys, ceramics, polymers and composites; development and analysis of advanced materials processing and deposition techniques; nondestructive evaluation, component failure analysis and reliability; fracture mechanics and stress corrosion; analysis and evaluation of materials at cryogenic and elevated temperatures; launch vehicle fluid mechanics, heat transfer and flight dynamics; aerothermodynamics; chemical and electric propulsion; environmental chemistry; combustion processes; spacecraft structural mechanics, space environment effects on materials, hardening and vulnerability assessment; contamination, thermal and structural control; lubrication and surface phenomena; microengineering technology and microinstrument development.

Space and Environment Technology Center: Magnetospheric, auroral and cosmic ray physics, wave-particle interactions, magnetospheric plasma waves; atmospheric and ionospheric physics, density and composition of the upper atmosphere, remote sensing using atmospheric radiation; solar physics, infrared astronomy, infrared signature analysis; effects of solar activity, magnetic storms and nuclear explosions on the earth's atmosphere, ionosphere and magnetosphere; effects of electromagnetic and particulate radiations on space systems; space instrumentation; propellant chemistry, chemical dynamics, environmental chemistry, trace detection; atmospheric chemical reactions, atmospheric optics, light scattering, state-specific chemical reactions and radiative signatures of missile plumes, and sensor out-of-field-of-view rejection.